Corrosion Resistance of AISI 316L Coated with an Air-Cured Hydrogen Silsesquioxane Based Spin-On-Glass Enamel in Chloride Environment

Lampert, Felix; Bruun Christiansen, Alexander ; Din, Rameez Ud; Gonzalez-Garcia, Yaiza ; Møller, Per

Published in:
Corrosion Science

Link to article, DOI:
10.1016/j.corsci.2017.08.024

Publication date:
2017

Document Version
Peer reviewed version

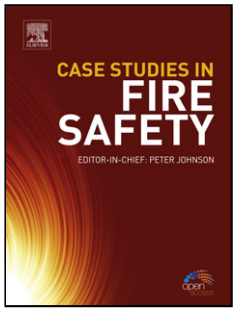

Title: Corrosion Resistance of AISI 316L Coated with an Air-Cured Hydrogen Silsesquioxane Based Spin-On-Glass Enamel in Chloride Environment

Authors: Felix Lampert, Alexander Bruun Christiansen, Rameez Ud Din, Yaiza Gonzalez-Garcia, Per Møller

PII: S0010-938X(17)30741-2
DOI: http://dx.doi.org/10.1016/j.corsci.2017.08.024
Reference: CS 7177

To appear in:

Received date: 24-4-2017
Revised date: 14-7-2017
Accepted date: 21-8-2017

Please cite this article as: Felix Lampert, Alexander Bruun Christiansen, Rameez Ud Din, Yaiza Gonzalez-Garcia, Per Møller, Corrosion Resistance of AISI 316L Coated with an Air-Cured Hydrogen Silsesquioxane Based Spin-On-Glass Enamel in Chloride Environment, Corrosion Sciencehttp://dx.doi.org/10.1016/j.corsci.2017.08.024

Corrosion Resistance of AISI 316L Coated with an Air-Cured Hydrogen Silsesquioxane Based Spin-On-Glass Enamel in Chloride Environment

Felix Lampert [a*], Alexander Bruun Christiansen [b], Rameez Ud Din [c], Yaiza Gonzalez-Garcia [d], Per Møller [e]

[a] Technical University of Denmark (DTU), Department of Mechanical Engineering, Produktionstorvet, Building 425, 2800 Kgs. Lyngby, Denmark, e-mail: felamp@mek.dtu.dk

[b] SiOx ApS, Bybjergvej 7, 3060 Espergærde, Denmark, e-mail: alexander@siox.dk

[c] Technical University of Denmark (DTU), Department of Mechanical Engineering, Produktionstorvet, Building 425, 2800 Kgs. Lyngby, Denmark, e-mail: rudin@mek.dtu.dk

[d] Delft University of Technology, Department of Materials Science and Engineering, 2628CD Delft, The Netherlands, e-mail: y.gonzalezgarcia@tudelft.nl

[e] Technical University of Denmark (DTU), Department of Mechanical Engineering, Nils Koppels Allé, Building 404, 2800 Kgs. Lyngby, Denmark, e-mail: pm@mek.dtu.dk

* Corresponding author: Felix Lampert, e-mail: felamp@mek.dtu.dk

Highlights

- The efficiency of HSQ-based barrier coatings on 316L substrate is investigated
- Excessive thermal oxidation of the substrate leads to coating failure
- The chemical coating stability increases with increasing coating polymerization
- Curing in air is inadequate for HSQ-based corrosion barrier coatings

Abstract

The efficiency of thin hydrogen silsesquioxane (HSQ) -based corrosion barrier coatings on 316L substrates after oxidative thermal curing at 400-550 ºC in air was investigated. Infrared spectroscopy and electrochemical impedance spectroscopy showed that an increasing curing temperature leads to progressing coating densification, accompanied by decreasing barrier properties. Cyclic polarization measurements indicated that defects due to substrate oxidation are detrimental for the substrate passivity. Insufficiently polymerized coatings showed poor chemical stability in neutral salt spray testing and the chemical coating stability increased with curing temperature. Oxidative curing was found inadequate as polymerization treatment of HSQ-based corrosion barrier coatings on 316L substrate.

Keywords: Stainless Steel, EIS, IR Spectroscopy, Polarisation, Oxide Coatings, Passivity

1 Introduction

Gasketed plate heat exchangers find application in generic heating/cooling systems and may find use in e.g. marine applications, which necessitates sufficient resistance of the plate materials towards corrosion in hot seawater. Due to the highly corrosive properties of the environment during service, the heat exchangers are typically fitted with Ti-alloy plates, which behave virtually inert in this environment. Despite the outstanding performance, the high price of the material gives an incentive to change from Ti-based plates to other plate materials such as stainless steels, which may yield a significant reduction in material cost under high volume production. However, stainless steels may be sensitive to localized corrosion in seawater [1–3] and the application of stainless steels as plate material in Cl^- containing media is highly compromised due to localized corrosive failure of the plates [4], triggering the need for costly, highly alloyed steels or advanced corrosion prevention strategies. Traditional corrosion protection concepts, such as organic coatings or vitreous enamels, impair the heat transfer over the plates and are not applicable for heat exchanger plates. Moreover, advanced corrosion protection concepts such as cathodic protection are challenging, due to the complex geometry of the assembled component, triggering the need for novel concepts to increase the lifetime of stainless steels in marine heat exchangers.

As a viable concept to prevent the corrosive failure of stainless steel components in saline environment, the deposition of micrometer/sub-micrometer –thick anti-corrosion coating films based on inorganic ceramics such as TiO_2 [5–8], Al_2O_3 [9] and SiO_x [10–14] or organic/inorganic hybrid materials [15] has been investigated. In particular, inert thin coating systems, i.e. ~ 50-600 nm based on SiO_x from chemical vapor deposition (CVD) or sol-gel processing have shown promising results in suppressing both corrosion in chloride [14,16] and acid media [10,11]. Similar to traditional vitreous enamels [17], which typically exhibit thicknesses at millimeter-scale, the

coating films act as a physical barrier between the substrate and the aggressive environment and show remarkable barrier properties towards ionic transport [14]. The application of thin film coating technology is of particular interest for heat exchangers, since it promises significant enhancements in material durability or resistance towards biofouling [18,19] at a minimum impairment of the heat transfer.

Despite their high potential, the applicability of the existing technologies is limited due to the high processing cost of CVD processes, which require a reactor and vacuum equipment [20], or the inherently porous nature of sol-gel SiO_2, which requires high temperature sintering (> 600 ºC) to reach fully densified ceramic films [21]. As a viable alternative to the traditional processes, the deposition of SiO_2-like films from hydrogen silsesquioxane (HSQ) precursor has been demonstrated [22–24]. Since the process relies on the deposition of a liquid precursor by e.g. spin-, dip- or spray- coating without the need for complex processing equipment, it shows significant economic advantages with respect to CVD processes together with a decrease in thermal budget with respect to sol-gel processes, since inherent film porosities collapse at curing temperatures around 435 ºC [22]. Recent investigations [25–31] validated the applicability of HSQ as precursor for sub-micrometer thick coatings on metallic substrates with a particular industrial interest as planarization treatment [25,26,29] or carrier of nanopatterns [28] for injection molding tools. In addition, HSQ-based thin films have shown to possess excellent barrier properties in aqueous solutions [31] and are promising precursors for the next generation of sub-micrometer thick barrier coatings.

HSQ-based spin-on-glass has been primarily developed for the application as low dielectric constant interlayer dielectric material for microelectronics [22–24]. To avoid the deterioration of the dielectric constant, leading to increased parasitic capacitance in interlayer dielectric

applications [32], the material needs to be thermally polymerized in oxygen-free atmosphere [23]. As discussed by Bremmer et al. [23], the introduction of oxygen to the curing atmosphere leads to a change in the predominant polymerization mechanism from a bond redistribution reaction to an oxidation/condensation of the precursor, yielding a higher curing efficiency of the process and, thus, a reduced thermal budget for oxidative curing. Despite the higher curing efficiency and decreased thermal budget of oxidative film curing [23], curing in oxygen-free environment has been adopted for coating applications [25,26,28,31], where an increase in dielectric constant does not impact the performance.

Our recent investigations [33], demonstrated the feasibility of oxidative curing of HSQ-based coatings on stainless steel substrates in air ambient at 450 ºC. The process yielded well adherent, sub-micrometer thick films with a stoichiometry close to SiO_2 and excellent substrate coverage. In contrast to curing in oxygen depleted environment [31], access to oxygen at the coating/metal interface led to thermal oxidation of the substrate, yielding a ~20-30 nm thick interface oxide in connection with a Cr-depleted zone in the substrate surface. The impact of the interfacial oxide and Cr depletion on the corrosion properties of oxidatively cured HSQ-based spin-on-glass coatings was not reported, however, it was suggested that it may compromise the advantages of the novel, more efficient curing process with respect to oxygen-free curing. Our previous investigation [31] on the anti-corrosion performance of HSQ-based coatings solely focused on non-oxidatively cured systems and, further, only assessed the coating barrier properties in pH-buffered solution for short immersion times. However, the successful implementation of the technology requires a detailed assessment of the coating barrier properties and polarization resistance in a technically relevant electrolyte such as NaCl solution as well as an assessment of

the long-term coating stability by standardized techniques such as salt spray testing, necessitating a detailed study of the material behavior as barrier coating in chloride environment.

Hence, the present work focuses on the microstructure, corrosion performance and evaluation of HSQ-based coatings on AISI 316L substrates in the curing temperature range from 400-550 ºC in air. The effect of the curing-temperature variation on the coating microstructure, chemistry and wetting is investigated using focused ion beam assisted scanning electron microscopy, infrared spectroscopy and water contact angle measurements, respectively. Moreover, the corrosion performance of coated substrates in chloride containing media is evaluated by cyclic polarization, electrochemical impedance spectroscopy, the scanning vibrating electrode technique and neutral salt spray testing.

2 Experimental

2.1 Thin film deposition

AISI 316L (Composition (wt%): 17.5 Cr, 10.5 Ni, 2.2 Mo, 1.2 Mn, 0.5 Si, bal. Fe; determined by Energy dispersive X-ray spectroscopy (EDS) at 20 kV acceleration voltage on a JEOL JSM-5900 Scanning Electron Microscope (SEM) with Oxford Instruments EDS detector) test coupons with no. 2B surface finish and dimension of 50 x 100 x 1 mm^3 have been coated with the commercial product Dow Corning FOx25 flowable oxide, which is a solution containing 22-23 wt.% HSQ, $(HSiO_{3/2})_n$, in a blend of $C_8H_{24}O_2Si_3$ with $C_6H_{18}OSi_2$ in a ratio of 1:3. The coating deposition was carried out in analogy to Lampert et al. [33], i.e. by dip-coating with 1 mm/s withdrawal speed, followed by a soft-baking step at 160 ºC for 30 min (leading to solvent evaporation) and a thermal polymerization cycle for 2 h in air, whereby the polymerization temperature was varied between

400 and 550 ºC. Prior to deposition, the metallic substrates were prepared by immersion degreasing in Schlötter Slotoclean AK 90, followed by anodic degreasing in Schlötter Slotoclean EL DCG at 8 A/dm^2 and acid picklilng in Schlötter Slotoclean Decasel 5. For thin film analysis by FT-IR, thin films were deposited on the front side of Si-wafers (Topsil FZ, 675 µm thickness, front side polished, backside etched) and cured in a similar fashion. In the following, the "uncured" sample condition refers to a soft-baked film deposited on Si-wafer substrate. The four different curing conditions of coatings on AISI 316L substrate will be denoted as "sample *curing temperature*", while uncoated, bare AISI 316L substrates will be denoted as "uncoated" reference.

2.2 Microstructure, Chemical and Electrochemical Characterization

2.2.1 Scanning Electron Microscopy (SEM)

SEM analysis was performed on a Helios Nanolab 600 dual beam SEM fitted with a field emission gun and a Ga^+ focused ion beam source. Cross-sections of coated samples were prepared by ion beam milling at 30 kV acceleration voltage and imaging on the trench wall under 52 º sample tilt. Prior to ion beam milling, the surface was protected by Pt deposition to minimize the effect of ion beam damage. All samples prepared for electron microscopy were sputter coated with an Au film of a few nanometers thickness to reduce the effect of surface charging. The microscope was operated at 5 kV acceleration voltage for SEM imaging. The further microscope settings, i.e. detector type (Everhart-Thornley detector (ETD) or Through Lens detector (TLD)) and beam current, are indicated in the respective figure captions.

2.2.2 Fourier Transformed Infrared Spectroscopy (FT-IR)

FT-IR data acquisition was carried out on a Thermo Scientific Nicolet iN10 MX on thin films deposited on Si-wafer. All measurements were performed in transmission mode, whereby the

background was acquired on a Si-wafer. Quantification of the Si-H ratio was done by integration of the Si-H stretching edge on a linear background and the reported residual Si-H ratio is the peak area normalized by the peak area of a soft baked, uncured film.

2.2.3 Water contact angle

Water contact angles were determined on the coated AISI 316L substrates on a ramé-hart instrument co. water contact angle goniometer by the sessile drop method with a droplet volume of 10 µl of purified water at room temperature. The reported values are averaged over 3 individual measurements.

2.2.4 Anodic cyclic potentiodynamic polarization (anodic CP)

The coated test coupons were investigated by cyclic potentiodynamic anodic polarization (CP) in pH neutral 3.5 wt.% aqueous NaCl solution on an ACM Instruments GillAC potentiostat. Anodic CP experiments were conducted in a flat corrosion cell with the cell design from Qvarfort [34]. The measurements were performed on an area of 1 cm^2 and a solution volume of 400 ml against a KCl saturated silver chloride (Ag-AgCl) reference electrode. Anodic CP-scans were performed after a cell-settle time of 3600 s with a scan rate of 1 mV/s. The experiments were repeated 3 times for consistency.

2.2.5 Scanning Vibrating Electrode Technique (SVET)

SVET analysis was carried out on an Applicable Electronics system, which was fitted with a platinized Pt/Ir-alloy vibrating probe and platinized Pt/Ir-alloy reference and ground electrodes. The probe diameter after platinization in 10 vol.% $PtCl_2$ + 1 vol.% $Pb(C_2H_3O_2)_2$ aqueous solution was ~ 30 µm. The probe capacitance was monitored before each experiment and kept above 2 nF. The sample surface was masked with a nonconductive varnish and the system was operated on the

freely corroding surface with an average probe working distance of 100 µm in a solution volume of 2 ml. Since no sufficiently high corrosion rates could be obtained in NaCl aqueous solutions without external polarization, the experiments were carried out in an aqueous solution of 1 wt.% $FeCl_3*H_2O$ with pH ~ 2 and solution resistivity of 82.03 Ωcm (determined on a Radiometer Copenhagen CDM 80 conductivity meter). The SVET maps were acquired with a size of 2.1 x 2.1 mm^2 at a resolution of 31 x 31 points, yielding a scan-rate of 20 minutes/map.

2.2.6 Electrochemical Impedance Spectroscopy (EIS)

EIS was performed on a Gamry Ref600 potentiostat in a flat, gasketed corrosion cell with 2.1 cm^2 area and 15 ml solution volume of neutral 3.5 wt.% NaCl aqueous solution. The potential was measured against a saturated calomel electrode and perturbed by a Pt-wire auxiliary electrode with an amplitude of $\pm$10 mV around the corrosion potential. The cell settle time prior to EIS measurements was 3600 s. Data analysis was carried out by equivalent circuit fitting with the commercial software Gamry Echem Analyst V 6.31 by the simplex method. The experimental data were validated by an automatic Kramers-Kronig test and all experiments were repeated 5 times to ensure consistency.

2.2.7 Neutral salt spray testing

Two redundant sets of samples were investigated by neutral salt spray testing in an Erichsen Corrocompact Model 612 corrosion testing apparatus. The tests were performed in accordance to EN ISO 9227:2012 [35] and discontinued after 1000 h due to severe failure of the coatings.

3 Results and Discussion

3.1 Visual appearance and microstructure

Digital photographs of half-coated test coupons are shown in Figure 1. In general, the coated part of the coupons shows distinct discoloration, i.e. blue/golden, yellow/golden and brown/golden depending on the curing temperature, while the uncoated part of the coupons is tarnished due to thermal oxidation.

Similar to previous investigations [31,33], the coatings show good coverage and leveling via flowing into sub-micrometer substrate defects (Figure 2), leading to an inhomogeneous thickness distribution with a minimum thickness of ~ 200 nm, as indicated in the subfigures of Figure 2. Furthermore, the coatings on samples 400 and 450 are well adherent (Figure 2(a,b)), whereas voids at the metal-coating interface are observed for samples 500 and 550 (Figure 2(c,d)). All samples show a distinct interface layer at the metal-coating interface (indicated by "interface" in Figure 2), which increases in thickness with increasing curing temperature. As previously shown for sample 450 [33], the interface is composed of transition metal oxides from the thermal oxidation of the substrate and, in analogy, it can be assumed that the interface layers are predominantly formed by the thermal oxidation of the substrate.

3.2 Film chemistry

The chemistry and degree of cross-linking of HSQ-based thin films is frequently characterized by FT-IR [22,23,36]. An FT-IR absorption plot for an uncured reference film along with the cured film conditions is shown in Figure 3, whereby the identification of the FT-IR spectral features was carried out according to the edge positions summarized in Table 1. As shown in Figure 3, the FT-IR absorption spectrum of uncured HSQ is dominated by pronounced absorption from Si-H

stretching and Si-O asymmetric stretching in cage structure while neither silanol nor water can be detected. Curing between 400 and 550 ºC leads to a clear shift in Si-O asymmetric stretching from 1140 cm^{-1} to 1075 cm^{-1}, together with a loss in absorption from Si-H stretching, indicating progressive polymerization of the films [36]. In addition to Si-H stretching at 2260-2285 cm^{-1}, a Si-H pre-edge at 2200 cm^{-1} appears for curing at 400 ºC, indicating the presence of intermediate reaction products between HSQ and SiO_2 and, hence, incomplete polymerization of the film [37]. The more polymerized films do not show the presence of the Si-H pre-edge.

The degree of polymerization was quantified via the loss in integrated Si-H stretching absorption intensity, as proposed in previous works [22,23]. A plot depicting the residual Si-H absorption vs. curing temperature is shown in Figure 3b. It is evident that an increase in curing temperature reduces the amount of remaining Si-H stretching absorption intensity from 39.5 % at 400 ºC curing to 0 % at 550 ºC curing. As established by Bremmer et al. [23], the film density increases with decreasing remaining Si-H ratio for oxidatively cured HSQ films. Based on extrapolation of their data, the films cured at 400 ºC (residual Si-H of 40 %) are expected to have a film density of ~ 75 % of thermal SiO_2, while the films cured at 450 ºC (residual Si-H of 17 %) are expected to have a density of ~ 80 % of thermal SiO_2. A further increase in film density for the higher curing temperatures is expected, however, the herein reported remaining Si-H ratios are out of the data range reported by Bremmer et al. [23] and, hence, cannot be extrapolated.

Apart from IR-absorption due to HSQ in its respective degrees of polymerization, significant absorption from hydroxyl stretching due to silanol and molecular water is observed above 3000 cm^{-1} for all cured films and the integrated intensity of the hydroxyl stretching features, which is indicative for the amount of silanol present [38], is plotted vs. the curing temperature in Figure 3b.

Clearly, the amount of hydroxyl climaxes for curing at 450 ºC and declines for curing at higher temperatures, while the amount of hydroxyl is significantly decreased for the film cured at 400 ºC.

3.3 Coating hydrophobicity

The effect of the coating chemistry on the coating hydrophobicity was investigated via water contact angle measurements and the relation of water contact angle vs. curing temperature, is shown in Figure 4. Overall, all coatings are hydrophilic, however, sample 400 shows an increased contact angle with respect to the other samples. While residual non-polar Si-H repels water, polar silanol allows hydrogen-bonding to water [39] and thus, the affinity of HSQ-based films to water is controlled by a competition between silanol and residual Si-H [23]. Hence, weakly polymerized films, as observed from the FT-IR analysis of sample 400, have a high remaining Si-H ratio in combination with a high water contact angle, as opposed to more polymerized films, which, in consequence, show a higher hydrophilicity.

3.4 Potentiodynamic CP testing

The anodic CP behavior of the coated samples allows an assessment of the electrochemical properties of the substrate at coating defects such as cracks, pores or pinholes. As pointed out by other authors [14], the corrosion potential of coated stainless steels is largely determined by local differences in the concentration of reactive species in microscopic coating defects. Hence, an analysis of the substrate properties based on the corrosion potential will be omitted in the following and the analysis will solely be based on the passive current and pitting potential. Representative anodic CP curves of the coated samples and an uncoated reference are shown in Figure 5a. Overall, the reference and the coated samples cured at lower temperatures, i.e. sample 400 and 450, show distinct passive regions with significantly decreased passive current densities. Moreover, sample

500 and 550 do not exhibit passive behavior and, hence, no distinct pitting potential is observed. As shown in Figure 5b, the pitting potential is not altered with respect to the reference for sample 400, while a negative shift in pitting potential is observed for sample 450.

The observed decrease in passive current density for samples 400 and 450 is in agreement with reported data for similar coating systems [13,14,40,41]. As concluded by Pech et al. [14,40], this decrease in corrosion current density is predominantly attributed to a decrease in exposed substrate surface area, i.e. high coating coverage. However, the successful application of thin barrier coatings on stainless steels requires both high coverage and substrate passivity at coating defects and positive conclusions about the coating performance may not be drawn solely based on the passive current density. In analogy to the present investigation, a decrease in breakdown potential has been previously reported for sol-gel coated stainless steels [42] and explained by severe sensitization from $M_{23}C_6$ precipitation during the high temperature treatment. However, due to the herein presented material choice of a low carbon variant of the type 316 stainless steel ($\leq$ 0.030 wt.% C [43]), severe material deterioration due to carbide precipitation may be ruled out within the applied temperature range and ageing time [44]. The microstructure- analysis in section 3.1 showed that curing at more elevated temperatures leads to the more pronounced formation of interface oxides, which is assumed to deplete the substrate subsurface in Cr [33] and, further, has a detrimental effect on the coating adhesion. Hence, in analogy to thermal oxidation of stainless steels [45,46], the observed loss in passivity for the high temperature cures can be associated with a process-induced chemical modification of the substrate surface, which compromises the resistance to localized corrosion at coating defects such as interface voids. This hypothesis is in agreement with Pech et al. [14], who have reported that the substrate passivity at microscopic coating effects is of utmost importance for the performance of SiO_x coated stainless steels. Thus,

curing above 450 ºC in air strongly affects the coating performance in chloride-media due to the pronounced loss in substrate passivity.

3.4.1 Electrochemical Impedance Spectroscopy

While anodic CP measurements give detailed information about the level of substrate passivity, EIS analysis by equivalent circuit fitting allows for a distinct analysis and quantitative assessment of the coating barrier properties and gives further insight into the correlation between the previously established differences in coating properties and the barrier efficiency. Representative EIS spectra of the coated samples with their respective equivalent circuit fits are shown in Figure 6a, together with data for an uncoated reference. Equivalent circuit fitting was performed based on the models derived in reported literature [31], i.e. with a Randle's equivalent circuit for the reference and an R-(Q(R-(Q(R-W)))) –type model (Figure 6b) for the coated samples. Capacitive elements were fit with constant phase elements and the conversion to equivalent capacitances was conducted according to the method reported by Hsu et al. [47]. Resulting from the equivalent circuit fit, the pore resistance, R_p, charge transfer resistance, R_{ct}, coating capacitance, C_{coat} and the double layer capacitance, C_{dl} are plotted vs. the curing temperature in Figure 7.

In general, a trend of decreasing R_p with increasing curing temperatures, indicating an inverse relation between curing temperature and barrier properties is observed. C_{coat} is a function of various factors as described by [48]:

$$C = \varepsilon_r \varepsilon_0 \frac{A}{d} \qquad (1)$$

where A is the measured area, d the coating thickness, ε_0 the dielectric permittivity of vacuum and ε_r the dielectric coating constant. Since all coatings show full coverage at insignificant difference in coating thickness (section 3.1), A and d can be regarded as constant and the factor of 2.5 between

the averaged coating capacitances of sample 400 and 550 likely originates from a change in dielectric constant due to higher coating density [23,49,50], formation of silanol [23] or water uptake [51–53] which was previously indicated by FT-IR and water contact angle analysis. R_{ct} is dependent on the substrate passivity and the exposed substrate surface area [40] and a clear decrease in the average R_{ct} is observed (Figure 7a), supporting the previously formulated hypothesis of a decreased substrate passivity or the increased exposed substrate area observed from Figure 2. Overall, the R_{ct}-values determined for the coated samples are higher than the average R_{ct} of the reference, which is in agreement with the decreased current density observed from CP experiments and supports the hypothesis that the exposed substrate surface is strongly reduced by the coating. Likewise, analysis of C_{dl} allows conclusion about the exposed substrate surface via Eq. 1. In the dataset presented in Figure 7c, the average C_{dl} steadily increases with curing temperature, indicating that curing at higher temperature allows a more efficient electrolyte penetration of the coating, thereby, in conjunction with the interface void-formation, increasing the exposed substrate surface. Overall, the results obtained by EIS indicate that the coating barrier performance does not primarily correlate with the film density, but rather is a complex relation between the film density, hydrophobicity and coating adhesion.

3.5 Localized corrosion assessment by the SVET

As indicated by the anodic CP measurements, the coated samples may suffer from localized breakdown in chloride containing electrolyte, however, a detailed understanding of the localized breakdown mechanism requires further insight into the microscopic mechanism of pit initiation in spin-on-glass coated stainless steels. Hence, the pit initiation and the anodic/cathodic activity of the coating system, the uncoated reference and samples 400 and 450 were studied in-situ and ex-

situ by the SVET in 1 wt.% $FeCl_3*6H_2O$ aqueous solution in combination with SEM analysis. The uncoated reference and sample 400 remained passive within a test period of 24 h. As visible from Figure 8a, sample 450 shows a clear response in form of localized anodic activity from emerging pits after ~ 2 h of immersion. Moreover, the anodic sites are not geometrically stable and freshly emerging sites are visible even after a prolonged immersion of ~ 12 h, as shown in Figure 8(b,c). On the contrary, the cathodic sites (indicated by arrows in Figure 8a) evolve in the early stage of the experiment and their positions remain stable over time.

A presumable anodic area is depicted in the SEM micrograph shown in Figure 9a. As indicated by the arrows, the site shows coating fractures of several tens of micrometers in length. Cross-sectional analysis by ion beam milling (along the dashed line in Figure 9a) reveals a local corrosion site which has presumably evolved around a microscopic coating defect and spread laterally to the defect underneath the coating (Figure 9b). The cathodic mechanism has been investigated based on the cathodic site labelled with "cat A" in Figure 8a. It has to be emphasized that, under the given test conditions, the test electrolyte contains Fe^{3+} as oxidant and that the reduction of Fe^{3+} to Fe^{2+} is the primary cathodic reaction. Hence, the cathodic mechanism in Fe^{3+}-free electrolyte may not agree with the observations made in this paragraph. As depicted in Figure 9c, the cathodic site is an approx. circular coating defect with diameter > 30 µm at which the coating has blistered or mostly collapsed. The cathodic site has been investigated by ion beam milling along the dashed line in Figure 9c and an ion beam milled cross-sectional micrograph is shown in Figure 9d. The micrograph reveals a large subsurface pit at which the coating has spalled off or partially collapsed. Hence, it can be concluded that large pits, which evolve early in the corrosion process, may re-passivate and consequently form the pronounced cathodic sites observed in Figure 8.

Based on this analysis, we propose the mechanism for unstable pit formation throughout the experiment as illustrated in Figure 10. In analogy to e.g. a resistive salt film [54], the coating serves as a stable pit cover, which helps to maintain an aggressive electrolyte [55] at the anodic site. Since stable pit growth is not observed during the course of the experiment, we suggest the rupture of the coating as terminating event. As the corrosion site increases in size, the coating ruptures, which consequently allows the dilution of the aggressive pit electrolyte by the less aggressive bulk solution and subsequently re-passivation of the active site.

3.6 Neutral salt spray testing

All of the previous techniques depict the corrosion properties of coated substrates after short immersion times (1 h of immersion prior to measurement for anodic CP and EIS or up to 24 h for SVET) and may, thus, not sufficiently illustrate the coating performance after prolonged immersion times. To test the long term coating stability, the samples have been exposed to a 1000 h neutral salt spray test according to EN ISO 9227:2012 [35]. Digital photographs of the sample surfaces after the test are shown in Figure 11. Areas of interest have been indicated with the letters A-D and respective micrographs are shown in Figure 12.

The reference sample shows corrosive failure in form of pitting in conjunction with red rust formation around the pits (Figure 11a and, in detail, Figure 12a). In contrast, the coated samples (Figure 11(b-e)), do not show the formation of single large pits and exhibit surface degradation, which is visible as discoloration. Moreover, the discoloration is uniform on sample 400 while samples 450-550 show incontinuous, spot-wise discoloration.

SEM analysis of sample 400 (Figure 12b) shows, that the coating has mostly dissolved and only partially remains along the grain boundary valleys. Sample 550, in contrast, shows an increased

coating stability with a high coating coverage after the test (Figure 12c). As exemplarily shown for sample 450 (Figure 12d), the spot-wise discoloration originates from the agglomeration of micrometer-scale corrosion pits. Cross-sectional analysis (Figure 12e) of the area shown in Figure 12d reveals partial coating dissolution, which, however, appears less uniform with respect to sample 400. Moreover, local coating delamination in connection with the initiation of localized corrosion under the coating can be observed.

Overall, the visual analysis of the coupons (Figure 11) indicates more severe corrosive attack for the high temperature cured samples with respect to the low temperature cures or the reference. This observation is in agreement with the previous results, where a decrease in passive and barrier properties combined with coating delamination and more efficient electrolyte penetration due to an increased hydrophilicity was observed for the high temperature cures, which may have triggered a more rapid degradation of the substrate in the accelerated corrosion test. The inferior dissolution of the coatings cured at higher temperature can be accounted to a higher film density and degree of polymerization, which may induce a more advanced chemical stability of the coatings. These results are in agreement with reported data [56,57], where SiO_x films with poor polymerization and high defect density showed higher dissolution rates in neutral aqueous solutions. Further, the considerable amount of easily hydrolyzed residual Si-H moieties indicated by the FT-IR analysis in the low temperature cures may contribute to the coating instability [58].

4 Conclusions

Coatings cured at 400-450 ºC exhibit good adhesion, while void formation due to excessive thermal oxidation of the substrate can be observed for coatings cured at higher temperatures. The coating hydrophobicity correlates with the residual Si-H and silanol content and, consequently,

coatings cured below 450 ºC show a significantly higher hydrophobicity with respect to coatings cured at higher temperature. Moreover, the coating barrier properties are primarily dominated by the coating hydrophobicity and do not increase for increased coating densities. Further, the coating may act as stable pit cover and, hence, actively support stable pit growth. Overall, it is evident that air curing of HSQ-based coatings on AISI 316L substrate yields unfavorable properties of either the coating or the substrate. While curing at 400 ºC does not impair the passive character of the substrate, curing above 400 ºC adversely affects the substrate passivity, leading to a complete loss of passivity for curing above 450 ºC. Furthermore, a high defect density, poor cross-linking and high residual Si-H content impair the chemical stability of the coatings cured at low temperatures in neutral solution. Hence, curing in air ambient is an inefficient curing method for HSQ-based barrier coatings on AISI 316L substrate. Exclusion of oxygen in the curing atmosphere may eliminate the issues associated with substrate oxidation and, thus, enable higher curing temperatures and more advanced cross-linking without an impairment of the substrate passivity.

Acknowledgements

The authors acknowledge SiOx Aps for the deposition of coatings and all other project partners. Further, Innovation Fund Denmark is acknowledged for providing financial support for the project Q-HEX under grant number 50-2014-1.

References

[1] N.J. Laycock, J. Stewart, R.C. Newman, The Initiation of Crevice Corrosion in Stainless Steel, Corros. Sci. 39 (1997) 1791–1809.

[2] Z. Szklarska-Smialowska, J. Mankowski, Crevice Corrosion of Stainless Steels in Sodium Chloride Solution, Corros. Sci. 18 (1978) 953–960.

[3] M. Torkar, F. Tehovnik, M. Godec, Crevice corrosion of stainless-steel fastening components in an indoor marine-water basin, Mater. Technol. 46 (2012) 423–427.

[4] K.M. Deen, M. a. Virk, C.I. Haque, R. Ahmad, I.H. Khan, Failure investigation of heat exchanger plates due to pitting corrosion, Eng. Fail. Anal. 17 (2010) 886–893.

[5] L. Ćurković, H.O. Ćurković, S. Salopek, M.M. Renjo, S. Šegota, Enhancement of corrosion protection of AISI 304 stainless steel by nanostructured sol–gel TiO2 films, Corros. Sci. 77 (2013) 176–184.

[6] S. Li, J. Fu, Improvement in corrosion protection properties of TiO2 coatings by chromium doping, Corros. Sci. 68 (2013) 101–110.

[7] S.T. Döşlü, B.D. Mert, B. Yazıcı, Polyindole top coat on TiO2 sol–gel films for corrosion protection of steel, Corros. Sci. 66 (2013) 51–58.

[8] S. Meth, N. Savchenko, M. Koltypin, D. Starosvetsky, F.A. Viva, A. Groysman, C.N. Sukenik, Corrosion studies of stainless steel protected by a TiO2 thin film deposited on a sulfonate-functionalized self-assembled monolayer, Corros. Sci. 52 (2010) 125–129.

[9] G. Ruhi, O.P. Modi, I.B. Singh, Pitting of AISI 304L stainless steel coated with nano structured sol–gel alumina coatings in chloride containing acidic environments, Corros. Sci. 51 (2009) 3057–3063.

[10] D.C.L. Vasconcelos, J.A.N. Carvalho, M. Mantel, W.L. Vasconcelos, Corrosion resistance of stainless steel coated with sol–gel silica, J. Non. Cryst. Solids. 273 (2000) 135–139.

[11] M. Atik, P. de Lima Neto, L.A. Avaca, M.A. Aegerter, J. Zarzycki, Protection of 316L stainless steel against corrosion by SiO2 coatings, J. Mater. Sci. Lett. 13 (1994) 1081–1085.

[12] O. de Sanctis, L. Gomez, N. Pellegri, C. Parodi, A. Marajofsky, A. Duran, Protective Glass Coatings on Metallic Substrates, J. Non. Cryst. Solids. 121 (1990) 338–343.

[13] T. Hwang, H. Lee, H. Kim, G. Kim, Two layered silica protective film made by a spray-and-dip coating method on 304 stainless steel, J. Sol-Gel Sci. Technol. 55 (2010) 207–212.

[14] D. Pech, P. Steyer, J.-P. Millet, Electrochemical behaviour enhancement of stainless steels by a SiO2 PACVD coating, Corros. Sci. 50 (2008) 1492–1497.

[15] T. Wang, J. He, D. Sun, J. Zhou, Y. Guo, X. Ding, S. Wu, J. Zhao, J. Tang, Fabrication of continuous mesoporous organic–inorganic nanocomposite films for corrosion protection of stainless steel in PEM fuel cells, Corros. Sci. 53 (2011) 1498–1504.

[16] R.F.S. Lenza, W.L. Vasconcelos, Synthesis and properties of microporous sol–gel silica membranes, J. Non. Cryst. Solids. 273 (2000) 164–169.

[17] P. Møller, L.P. Nielsen, Vitreous Enamel, in: Adv. Surf. Technol. Vol 2, 2013: pp. 645–654.

[18] R. Rosmaninho, O. Santos, T. Nylander, M. Paulsson, M. Beuf, T. Benezech, S. Yiantsios, N. Andritsos, A. Karabelas, G. Rizzo, H. Müller-Steinhagen, L.F. Melo, Modified stainless steel surfaces targeted to reduce fouling – Evaluation of fouling by milk components, J. Food Eng. 80 (2007) 1176–1187.

[19] O. Santos, T. Nylander, R. Rosmaninho, G. Rizzo, S. Yiantsios, N. Andritsos, A. Karabelas,

H. Müller-Steinhagen, L. Melo, L. Boulangé-Petermann, C. Gabet, A. Braem, C. Trägårdh, M. Paulsson, Modified stainless steel surfaces targeted to reduce fouling—surface characterization, J. Food Eng. 64 (2004) 63–79.

[20] J. Foggiato, Chemical Vapor Deposition of Silicon Dioxide Films, in: Handb. Thin Film Depos. Process. Tech. (Second Ed., 2nd ed., Elsevier B.V., 2001: pp. 111–149.

[21] C.J. Brinker, G.W. Scherer, Sintering, in: Sol-Gel Sci., Academic Press, Inc., San Diego, 1990: pp. 675–742.

[22] Y.K. Siew, G. Sarkar, X. Hu, J. Hui, A. See, C.T. Chua, Thermal Curing of Hydrogen Silsesquioxane, J. Electrochem. Soc. 147 (2000) 335.

[23] J.N. Bremmer, Y. Liu, K.G. Gruszynski, F.C. Dall, Cure of Hydrogen Silsesquioxane for Intermetal Dielectric Applications, Mater. Res. Soc. Symp. Proc. 476 (1997) 37–44.

[24] M.J. Loboda, C.M. Grove, R.F. Schneider, Properties of a-SiOx:H Thin Films Deposited form Hydrogen Silsesquioxane Resins, J. Electrochem. Soc. 145 (1998) 2861–2866.

[25] K. Mohaghegh, H.N. Hansen, H. Pranov, G. Kofod, A study on the surface roughness of a thin HSQ coating on a fine milled surface, in: 14th Euspen Int. Conf. - Dubrovink, 2014.

[26] K. Mohaghegh, H.N. Hansen, H. Pranov, G. Kofod, Verification of thickness and surface roughness of a thin film transparent coating, in: Proc. 13th Euspen Int. Conf., Berlin, 2013.

[27] H. Pranov, Spin-on-glass assisted polishing of rough substrates, WO 2013/083129 A1, 2013.

[28] J. Cech, H. Pranov, G. Kofod, M. Matschuk, S. Murthy, R. Taboryski, Surface roughness reduction using spray-coated hydrogen silsesquioxane reflow, Appl. Surf. Sci. 280 (2013) 424–430.

[29] T.C. Hobæk, M. Matschuk, J. Kafka, H.J. Pranov, N.B. Larsen, Hydrogen silsesquioxane mold coatings for improved replication of nanopatterns by injection molding, J. Micromechanics Microengineering. 25 (2015) 035018 (9pp).

[30] H. Pranov, Reactive Silicon Oxide Precursor Facilitated Anti-Corrosion Treatment, US 2014/0154441 A1, USA, 2014.

[31] F. Lampert, A.H. Jensen, R.U. Din, P. Møller, Hydrogen Silsesquioxane based silica glass coatings for the corrosion protection of austenitic stainless steel, Surf. Coatings Technol. 307 (2016) 879–885.

[32] P. Kohl, Low-dielectric constant insulators for future integrated circuits and packages, Annu. Rev. Chem. Biomol. Eng. 2 (2011) 379–401.

[33] F. Lampert, S. Kadkhodazadeh, A.H. Jensen, R.U. Din, P. Møller, Interfacial Interaction of Oxidatively Cured Hydrogen Silsesquioxane Spin-On-Glass Enamel with Stainless Steel Substrate, J. Electrochem. Soc. 164 (2017) C231–C239.

[34] R. Qvarfort, New Electrochemical Cell for Pitting Corrosion Testing, Corros. Sci. 28 (1988).

[35] EN ISO 9227:2012 Corrosion tests in artificial atmospheres - Salt spray tests, (2012).

[36] C.L. Frye, W.T. Collins, The Oligomeric Silsesquioxanes, (HSiO3/2)n, J. Am. Chem. Soc.

92 (1970) 5586–5588.

[37] M.G. Albrecht, C. Blanchette, Materials Issues with Thin Film Hydrogen Silsesquioxane Low K Dielectrics, J. Electrochem. Soc. 145 (1998) 4019–4025.

[38] W.A. Pliskin, Comparison of properties of dielectric films deposited by various methods, J. Vac. Sci. Technol. 14 (1977) 1064.

[39] W. Hertl, M.L. Hair, Adsorption of Water on Silica, Nature. 223 (1969) 1150–1151.

[40] D. Pech, P. Steyer, A.-S. Loir, J.C. Sánchez-López, J.-P. Millet, Analysis of the corrosion protective ability of PACVD silica-based coatings deposited on steel, Surf. Coatings Technol. 201 (2006) 347–352.

[41] B. Nikrooz, M. Zandrahimi, H. Ebrahimifar, High temperature oxidation resistance and corrosion properties of dip coated silica coating by sol gel method on stainless steel, J. Sol-Gel Sci. Technol. 63 (2012) 286–293.

[42] P.P. Trazaskoma-Paulette, A. Nazeri, Effects of Sol-Gel Coatings on the Localized Corrosion Behavior of 304 Stainless Steel, J. Electrochem. Soc. 144 (1997) 1307–1310.

[43] Designation: A959-16 Standard Guide for Specifying Harmonized Standard Grade Compositions for Wrought Stainless Steels, 2016.

[44] A. Kriaa, N. Hamdi, H. Sidhom, Assessment of Intergranular Corrosion of Heat Treated Austenitic Stainless Steel (AISI 316L Grade) by Electron Microscopy and Electrochemical Tests, Prot. Met. 44 (2008) 506–513.

[45] G. Hultquist, C. Leygraf, Selective Oxidation of a Ferritic Stainless Steel and its Influence on Resistance to Crevice Corrosion Initiation, Corros. Sci. 21 (1981) 401–408.

[46] F. Elshawesh, A. Elhoud, Role of heat tint on pitting corrosion of 304 austenitic stainless steel in chloride environment, in: Eur. Corros. Conf. Long Term Predict. Model. Corros. EUROCORR 2004, 2004.

[47] C.H. Hsu, F. Mansfeld, Technical Note: Concerning the Conversion of the Constant Phase Element Parameter Y0 into a Capacitance, Corrosion. 57 (2001) 747–748.

[48] F. Mansfeld, H. Shih, H. Greene, C.H. Tsai, Analysis of EIS Data for Common Corrosion Processes, in: Electrochem. Impedance Anal. Interpret., 1993: pp. 37–53.

[49] Y. Toivola, J. Thurn, R.F. Cook, Structural, Electrical, and Mechanical Properties Development during Curing of Low-k Hydrogen Silsesquioxane Films, J. Electrochem. Soc. 149 (2002) F9–F17.

[50] W.-C. Liu, C.-C. Yang, W.-C. Chen, B.-T. Dai, M.-S. Tsai, The structural transformation and properties of spin-on poly(silsesquioxane) films by thermal curing, J. Non. Cryst. Solids. 311 (2002) 233–240.

[51] D.M. Brasher, A.H. Kingsbury, Electrical Measurements in the Study of Immersed Paint Coatings on Metal. 1. Comparison between Capacitance and Gravimetric Methods of Estimating Water-Uptake, J. Appl. Chem. 4 (1954) 62–72.

[52] A.S. Castela, A.M. Simões, An impedance model for the estimation of water absorption in organic coatings. Part I: A linear dielectric mixture equation, Corros. Sci. 45 (2003) 1631–

1646.

[53] Lindqvist S.A., Theory of Dielectric Properties of Heterogeneous Substances Applied to Water in a Paint Film, Corros. - NACE. 41 (1985) 69–75.

[54] G.S. Frankel, L. Stockert, F. Hunkeler, H. Boehni, Metastable Pitting of Stainless Steel, Corros. - NACE. 43 (1987) 429–436.

[55] P.C. Pistorius, G.T. Burstein, Metastable pitting corrosion of stainless steel and the transition to stability, Philos. Trans. R. Soc. Ser. A. 341 (1992) 531–559.

[56] M. Klause, U. Rothhaar, M. Bicker, W. Ohling, Dissolution of thin SiO2-coatings – Characterization and evaluation, J. Non. Cryst. Solids. 356 (2010) 141–146.

[57] S.-K. Kang, S.-W. Hwang, H. Cheng, S. Yu, B.H. Kim, J.-H. Kim, Y. Huang, J.A. Rogers, Dissolution Behaviors and Applications of Silicon Oxides and Nitrides in Transient Electronics, Adv. Funct. Mater. 24 (2014) 4427–4434.

[58] C.J. Brinker, G.W. Scherer, Hyrdolysis and Condensation of Silicon Alkoxides, in: Sol-Gel Sci., Academic Press, Inc., San Diego, 1990: pp. 108–216.

[59] P. Innocenzi, Infrared spectroscopy of sol-gel derived silica-based films: A spectra-microstructure overview, J. Non. Cryst. Solids. 316 (2003) 309–319.

[60] P. Bornhauser, G. Calzaferri, Ring-Opening Vibrations of Spherosiloxanes, J. Phys. Chem. 100 (1996) 2035–2044.

[61] I.P. Lisovskii, V.G. Litovchenko, V.G. Lozinskii, G.I. Steblovskii, IR spectroscopic investigation of SiO2 film structure, Thin Solid Films. 213 (1992) 164–169.

[62] D.L. Olynick, B. Cord, A. Schipotinin, D.F. Ogletree, P.J. Schuck, Electron-beam exposure mechanisms in hydrogen silsesquioxane investigated by vibrational spectroscopy and in situ electron-beam-induced desorption, J. Vac. Sci. Technol. B Microelectron. Nanom. Struct. 28 (2010) 581–587.

[63] S.W. Bruun, A. Kohler, I. Adt, G.D. Sockalingum, M. Manfait, H. Martens, Correcting Attenuated Total Reflection – Fourier Transform Infrared Spectra for Water Vapor and Carbon Dioxide, Appl. Spectrosc. 60 (2006) 1029–1039.

[64] C.J. Brinker, G.W. Scherer, 2.4.3. IR-Raman investigations of gel dehydroxylation, in: Sol Gel Sci. Phys. Chem. Sol-Gel Process., 1990: pp. 582–588.

Tables

Table 1: FT-IR absorption edges expected in HSQ-based thin films (literature values)

Wavenumber [cm-1]	Description	Reference
795	Si-O symmetric stretching	[59]

830	Si-O bending	[37]
870	Si-H bending	[37,60]
1075	Si-O asymmetric stretching (incompletely closed cage moieties)	[36]
1140	Si-O asymmetric stretching (closed cage moieties)	[36]
1200-1300	Si-O asymmetric stretching (longitudinal optical splitting)	[59,61]
2200	Si-H stretching in $H_2SiO_{2/2}$	[37,62]
2260-2285	Si-H stretching in $HSiO_{3/2}$	[36]
2242-2208	C=O asymmetric stretching in atmospheric CO_2	[63]
3200-3500	O-H stretching of hydrogen bonded hydroxyl	[59,64]
3660	O-H stretching in Si-OH	[59,64]

Figure Captions

Figure 1: Digital photographs of test coupons (size 100x50 mm^2) with coated (c.) and uncoated (unc.) parts after curing at: (a) 400 ˚C; (b) 450 ˚C; (c) 500 ˚C; (d) 550 ˚C.

Figure 2: SEM images of FIB-milled cross-sections: samples cured at (a) 400 ˚C; (b) 450 ˚C; (c) 500 ˚C; (d) 550 ˚C. The areas have been coated with Au and Pt prior to milling. Microscope settings: TLD; beam current 86 pA.

Figure 3: (a) FT-IR absorption spectra of HSQ films deposited on Si wafer. The origin of the edges is summarized in Table 1. "Uncured" refers to an HSQ film which was soft-baked (dried at 160ºC for 30 min). The CO_2-edge is an atmospheric artefact. (b) Remaining percentage of Si-H based on the Si-H stretching absorption edges at 2260-2285 cm^{-1} and integrated intensity of hydroxyl stretching absorption between above 3000 cm^{-1}. 100 % remaining Si-H corresponds to the Si-H stretching absorption edge in a soft-baked HSQ film.

Figure 4: Water contact angle vs. curing temperature on coated AISI 316L substrates. The values represent average values of 3 measurements with the indicated standard deviation.

Figure 5: (a) Anodic CP curves in 3.5 wt.% NaCl in water. Sample 500 is excluded from the graph (due to similarity to sample 550). (b) Pitting potential vs. curing temperature. The values represent average values of 3 measurements with the indicated standard deviation.

Figure 6: (a) EIS Bode plots of test coupons in 3.5 wt.% NaCl. Solid lines are on the basis of the fitted model. (b) Schematic coating defect and respective equivalent circuit. With solution resistance R_s, charge transfer resistance R_{ct}, pore resistance R_p, constant phase element (CPE) of double layer Q_{dl}, CPE of coating Q_{coat} and Warburg element W.

Figure 7: Results of EIS fits vs. curing temperature: (a) Normalized pore/charge transfer resistance, R_p/R_{ct}; (b) Normalized coating capacitance, C_{coat}; (c) Normalized double layer capacitance, C_{dl}. The values represent average values of 5 measurements with the indicated standard deviation.

Figure 8: SVET contour plot of sample 450 in 1 wt.% $FeCl_3{*}6H_2O$ after (a) 2 h; (b) 11 h, 40min; (c) 12 h immersion. The framerate of the experiment was 1 frame / 20 min. The arrows indicate the positions of the cathodic sites. "cat A" indicates the acquisition-site for the SEM micrograph in Figure 9c.

Figure 9: Surface of sample 450 after SVET test: (a) SEM micrograph of anodic site in top-view. Microscope settings: ETD, beam current 0.69 nA; (b) cross-sectional view of detail FIB A. Microscope settings: TLD, beam current 86 pA; (c) SEM micrograph of cathodic site in top-view. The acquisition site is indicated with "cat A" in Figure 8a. Microscope settings: ETD, beam current 0.69 nA; (d) cross-sectional view of detail FIB B. Microscope settings: TLD, beam current 86 pA.

Figure 10: Illustration of corrosion mechanism in SVET experiment: (a) A major coating defect supports the cathodic reaction, while the coating acts as stable pit cover to maintain the aggressive pit electrolyte in a growing pit. (b) As the pit reaches a critical size, the coating ruptures, allowing electrolyte exchange of the pit and subsequently re-passivation of the surface.

Figure 11: Digital photographs of test coupons after 1000 h neutral salt spray testing: (a) reference; (b) sample 400; (c) sample 450; (d) sample 500; (e) sample 550. Detailed views of sites A-D are shown in Figure 12. The exposed sample area is 40x40 mm^2.

Figure 12: Detailed micrographs of areas indicated in Figure 11: (a) LOM of reference, pos. A; (b) SEM of sample 400, pos. B. Microscope settings: ETD, beam current 0.17 nA; (c) SEM sample

550, pos. C. Microscope settings: ETD, beam current 0.34 nA; (d) LOM of sample 450, pos. D; (e) cross-sectional view of the coating cross-section of sample 450, pos. D. Microscope settings: TLD, beam current 86 pA.

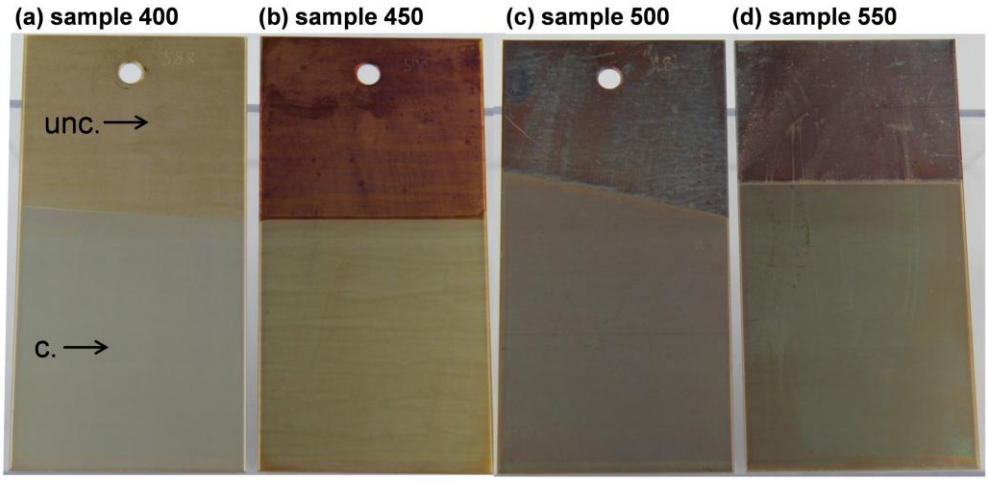

Figure 13

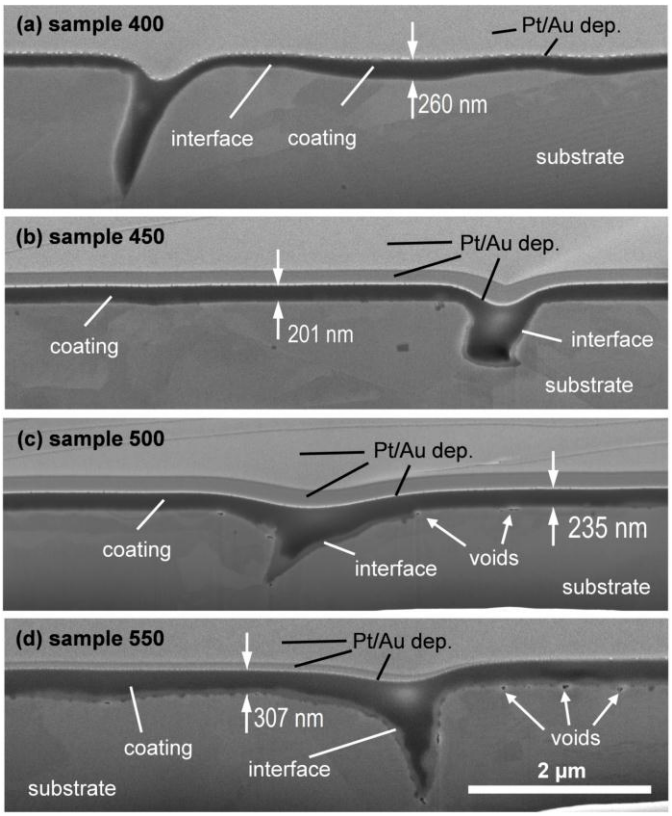

Figure 14

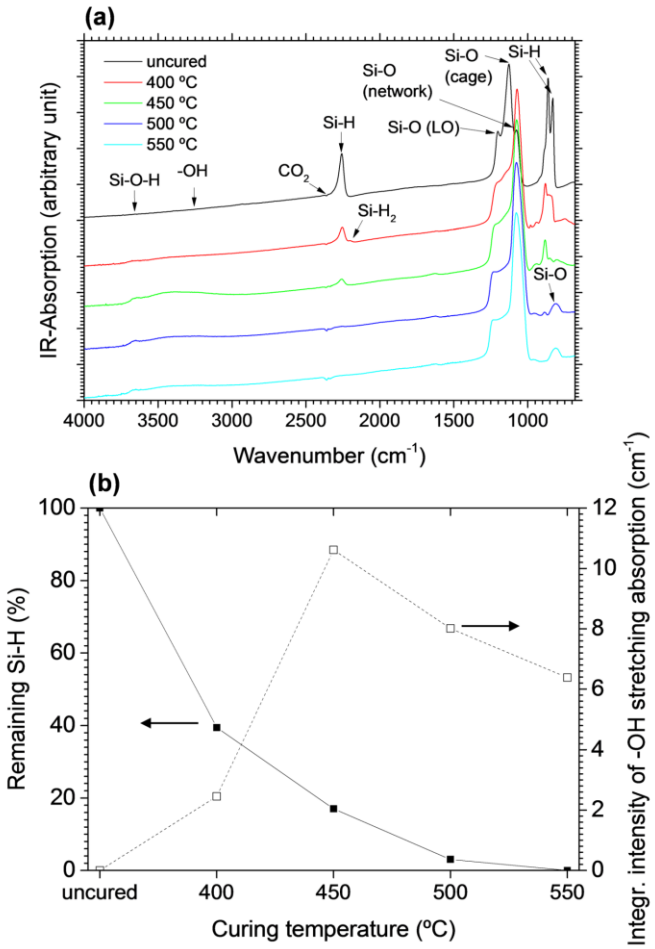

Figure 15

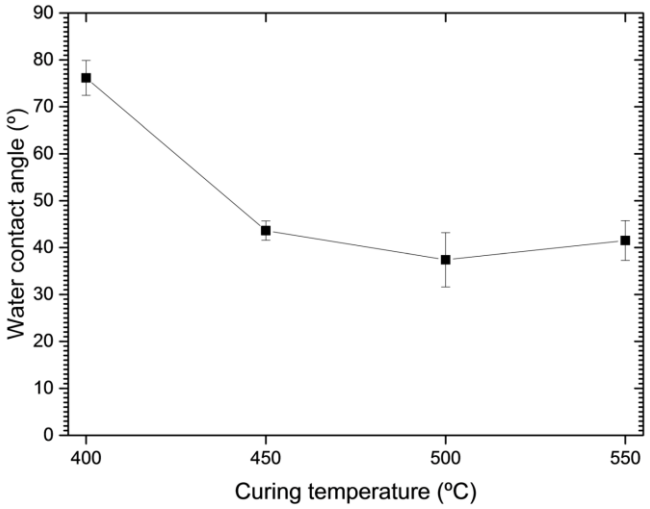

Figure 16

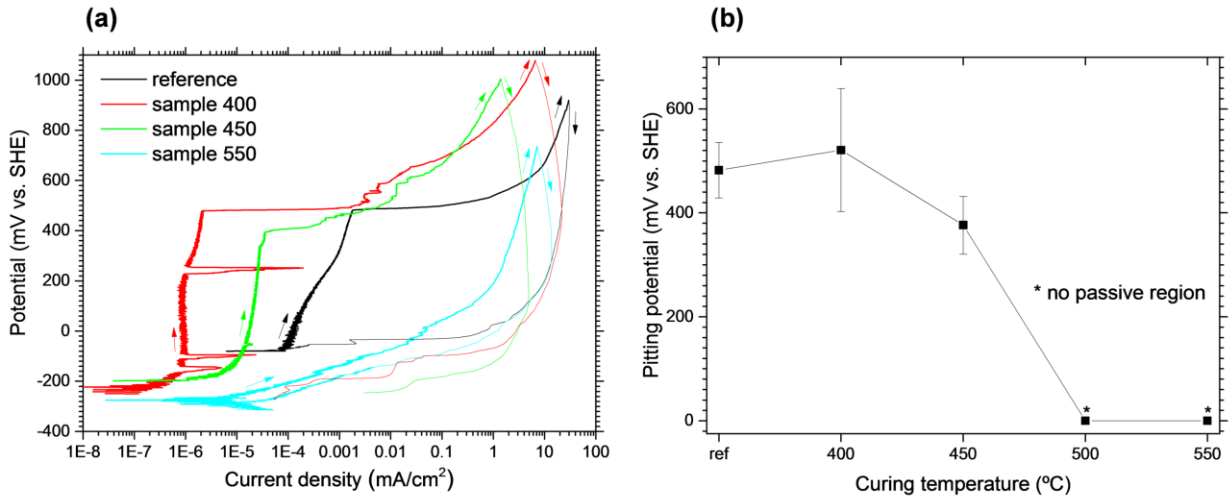

Figure 17

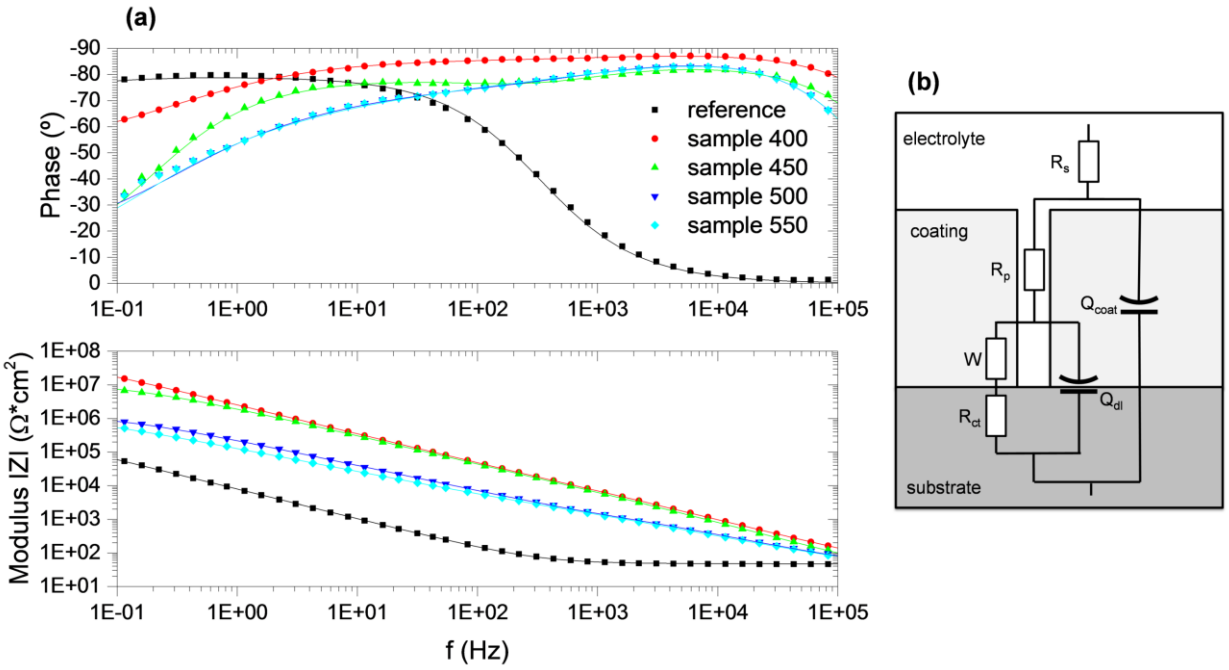

Figure 18

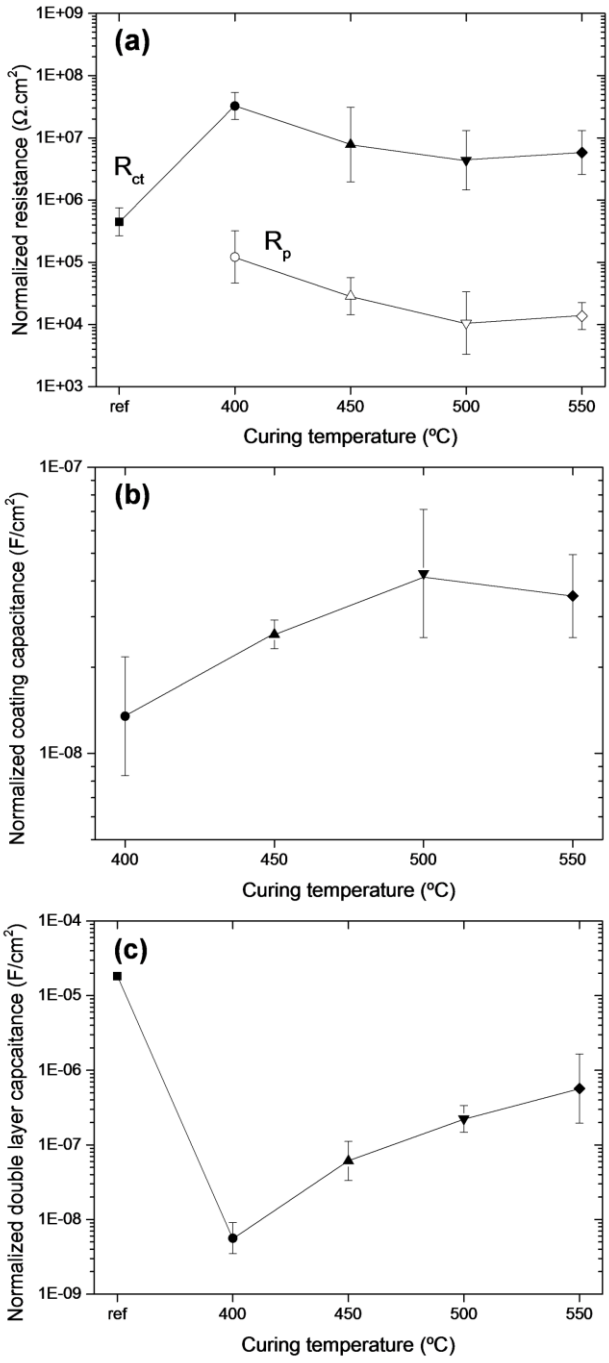

Figure 19

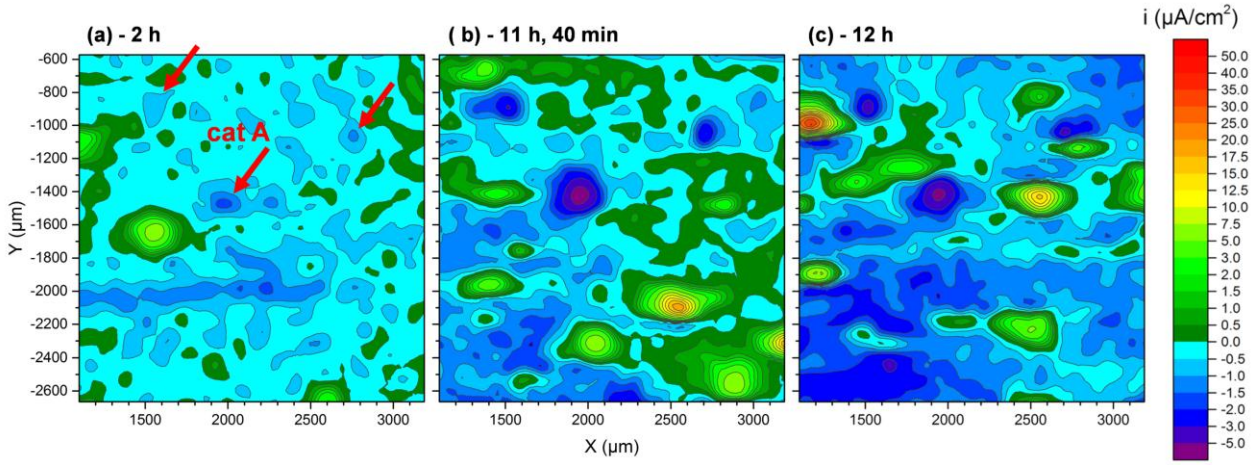

Figure 20

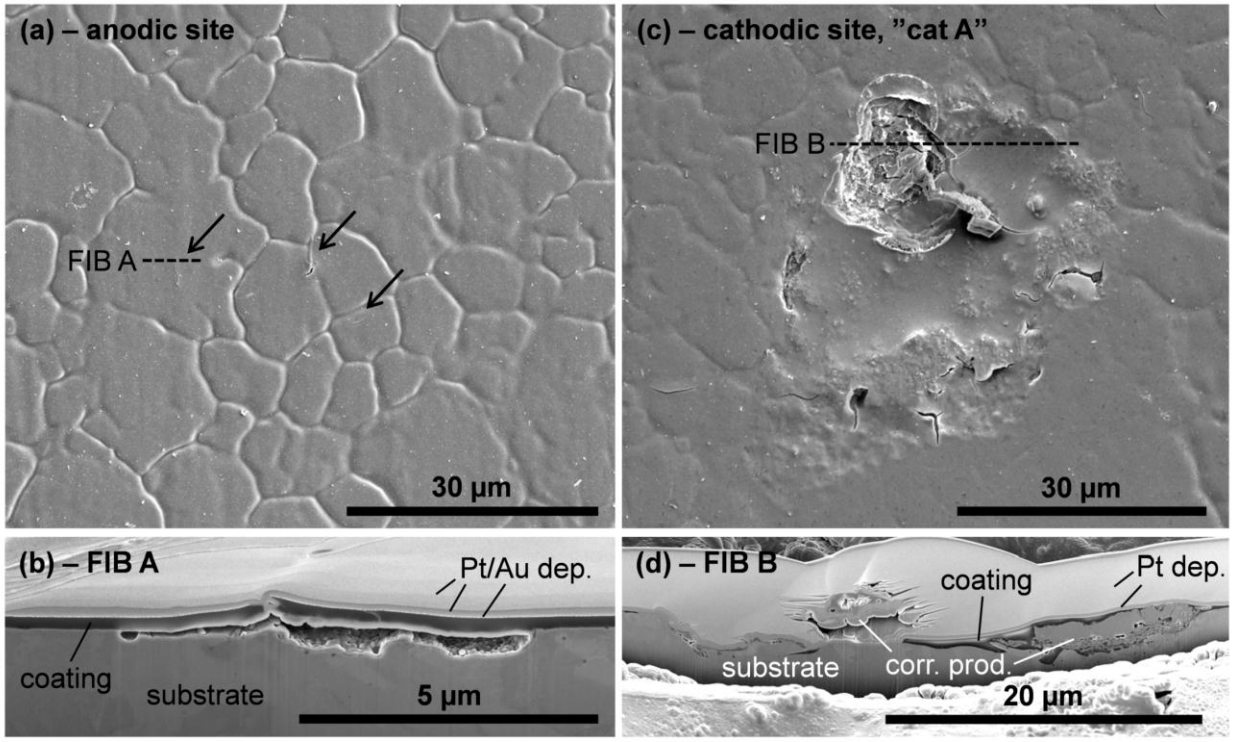

Figure 21

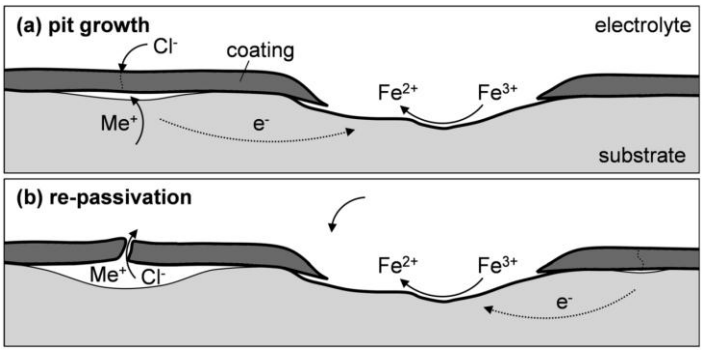

Figure 22

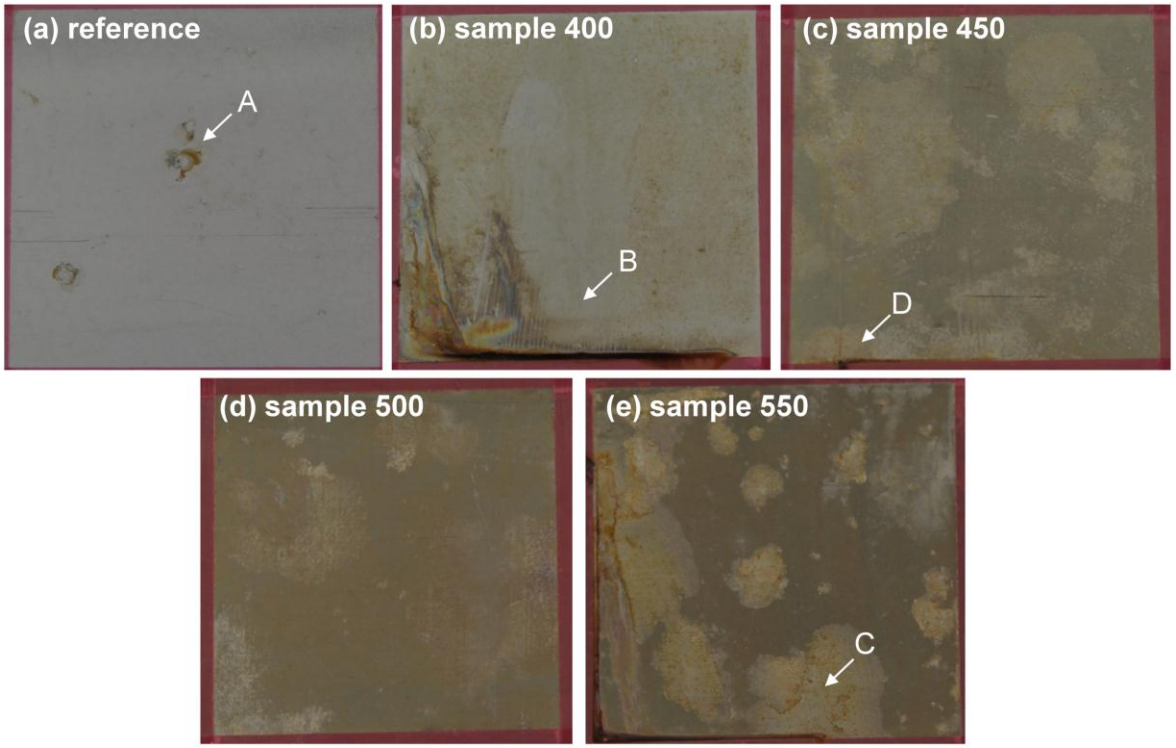

Figure 23

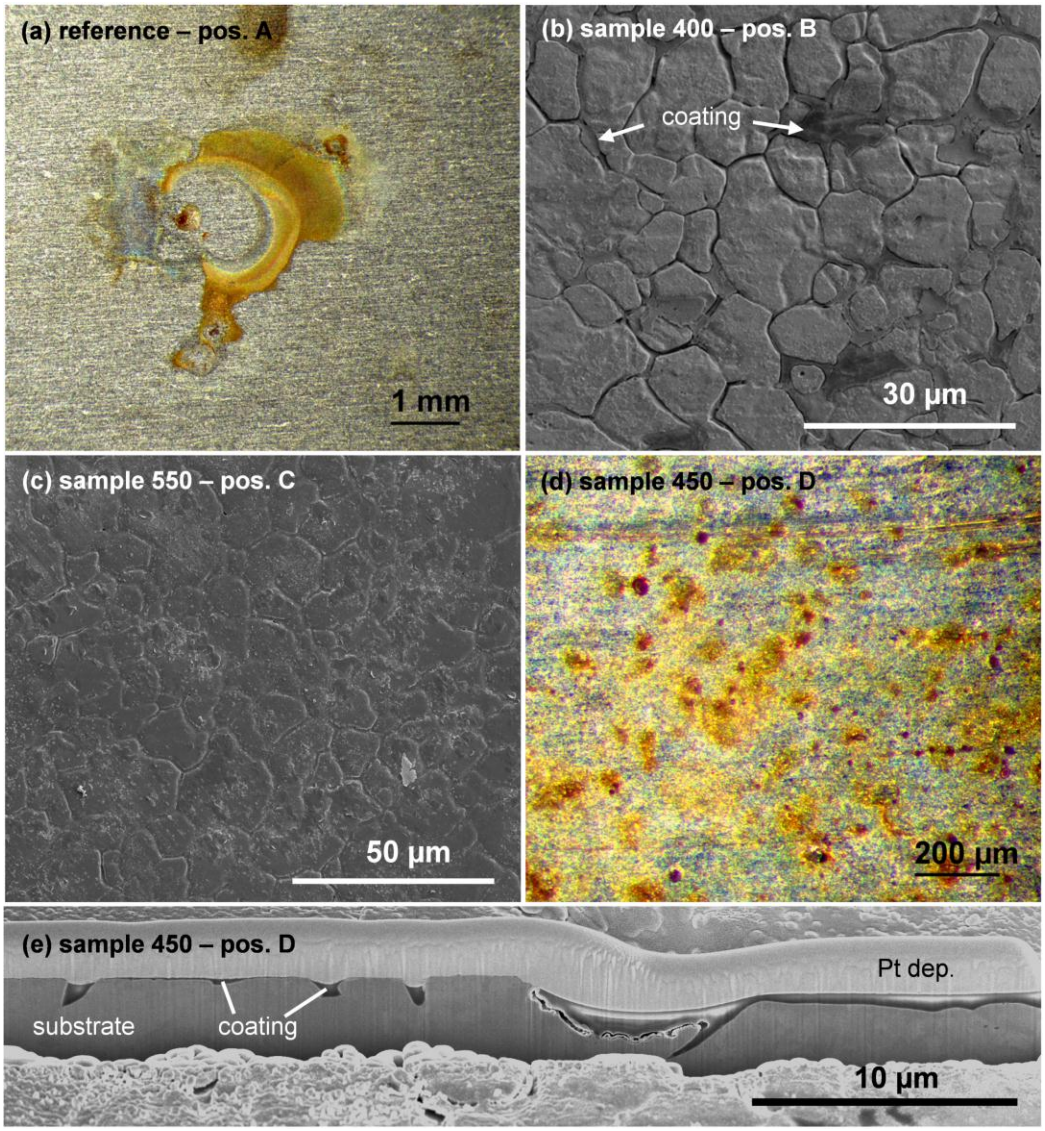

Figure 24